



Dynamics of magnetizations in the classical chaotic regime of the all-to-all Ising model with dissipation

Ni Zhihao,^{*} Qinhan Wu,^{*} Qian Wang , Xianlong Gao, and Pei Wang [†]

Department of Physics, Zhejiang Normal University, Jinhua 321004, People's Republic of China



(Received 20 February 2023; revised 16 November 2023; accepted 8 January 2024; published 31 January 2024)

We study the all-to-all Ising model in the presence of dissipation and periodic external field. The corresponding Lindblad equation has a time-periodic Liouvillian. The dynamics of magnetizations is explored by using both the mean-field theory and numerical simulation at a finite number of spins. The mean-field result exhibits a transition from the periodic response at small field amplitude to the chaotic dynamics at large amplitude. The Lyapunov exponents are calculated, which supports the existence of a classical chaotic phase. However, in the numerical simulation at a finite number of spins, the response is periodic at both small and large amplitudes. The scaling analysis of the Floquet Liouvillian spectrum suggests that the periodic response persists even in the thermodynamic limit. Further analysis shows that, in the classical chaotic regime, the density-matrix elements have a wide dispersion, instead of being localized. Such a delocalization of wave packets explains the failure of mean-field approximation.

DOI: [10.1103/PhysRevA.109.013328](https://doi.org/10.1103/PhysRevA.109.013328)

I. INTRODUCTION

Dissipative spin models are currently attracting wide interest, because they describe genuine nonequilibrium states of matter and, at the same time, can be realized in various platforms from superconducting circuits to Rydberg atoms [1–9]. The model consists of an ensemble of spins that are subject to dissipation caused by external baths. The dynamics are described by the Lindblad equation, obtained by integrating out the baths' degrees of freedom [10].

Great efforts have been taken in the investigation of various spin models. In the central spin model [11], the dissipative phase transition was located according to the closing of the Liouvillian gap. The transverse-field Ising model was thoroughly studied both under the mean-field approximation and beyond [12–17], in which the bistability of steady states in some region of the parameter space was found to be replaced by a first-order phase transition after the spatial correlation was correctly considered. As the couplings between spins are all-to-all couplings and then the system can be seen as a huge spin, the mean-field approximation was adopted. The magnetization was found to display an everlasting oscillation in the thermodynamic limit, indicating that the time translational symmetry is spontaneously broken into a discrete one [18–20]. If the dissipation acts in the eigenbasis of the transverse field, then a continuous dissipative phase transition manifests itself as continuous order parameters with discontinuous derivatives [21–24]. The XYZ-Heisenberg model was also studied by different approximation schemes [25–29] to clarify its phase diagram.

These studies focused on the time-independent Liouvillians. But much less is known as the Liouvillian changes periodically with time [30–40]. The topic of this paper is to study the response to a time-periodic Liouvillian. On the other hand, in closed quantum systems, the response to a time-periodic Hamiltonian has been under intensive investigations. The kicked top models were studied both theoretically [41–48] and experimentally [49–51], which is known to exhibit a transition between a regular dynamical phase and a chaotic one, depending on the value of the kicking strength. Similar chaotic behavior was found in the Lipkin-Meshkov-Glick model as the parameters change periodically with time [52–55]. The study in this paper can be seen as an investigation of the dissipation effect on the chaotic dynamics in the periodically driven spin models.

As a concise example, we study the all-to-all Ising model in the presence of collective dissipation. Without dissipation, chaotic behavior appears in the presence of a strongly oscillating external field [53–55]. We find that the chaotic behavior is robust against weak dissipation, if the mean-field approximation is taken. As the oscillating amplitude of field increases, a periodic response changes into a subharmonic oscillation, and then into a chaotic behavior. But the numerical simulation shows that, beyond the mean-field approximation, only the periodic response can survive the quantum fluctuation, but neither the subharmonic nor the chaotic dynamics can be observed. The mean-field approximation works only as the oscillating amplitude is small in the periodic-response regime, but it fails as the amplitude is large and describes chaos. Moreover, such a failure persists even if we consider the stochastic quantum trajectories. In some previous studies of dissipative quantum chaos [56–58], the dissipation localizes the wave packet, which is the foundation of mean-field approximation. But in our model, the wave packet is delocalized, explaining why the mean field fails.

^{*}These authors contributed equally to this work.

[†]wangpei@zjnu.cn

The paper is organized as follows. We introduce the model in Sec. II. Section III contributes to the discussion of the mean-field results. The exact numerical simulations of the dynamics of magnetizations are discussed in Sec. IV. In Sec. V, we explain the discrepancy between mean-field approximation and numerical results by looking into the density-matrix elements. The unraveling of the master equation and the corresponding quantum trajectories are discussed in Sec. VI. The Floquet Liouvillian spectrum is studied in Sec. VII. Finally, Sec. VIII summarizes our results.

II. THE MODEL

We consider the transverse field Ising model with all-to-all couplings, and a sinusoidal modulation added to the external field. The Hamiltonian is written as

$$\hat{H} = -Ng\hat{J}_x^2 + N\Gamma(t)\hat{J}_z, \quad (1)$$

where N denotes the total number of spins, g denotes the coupling strength, and $\hat{J}_\alpha = \sum_j \hat{\sigma}_j^\alpha / N$ denotes the collective spin operators with $\hat{\sigma}_j^\alpha$ being the Pauli matrices of the j th spin and $\alpha = x, y, z$. $\Gamma(t)$ denotes the time-dependent external field, which is supposed to be $\Gamma(t) = \Gamma_0 + A \sin(\omega_0 t)$, where A , Γ_0 , and ω_0 are the oscillating amplitude, mean value, and frequency, respectively. We set $g = 1$ as the unit of energy throughout the paper.

In the presence of dissipation, the dynamics of the system is described by the Lindblad equation [59]. The density matrix satisfies

$$\frac{d\hat{\rho}}{dt} = -i[\hat{H}, \hat{\rho}] + N\gamma_c(2\hat{J}_- \hat{\rho} \hat{J}_+ - \{\hat{\rho}, \hat{J}_+ \hat{J}_-\}), \quad (2)$$

where $\hat{J}_\pm = (\hat{J}_x \pm i\hat{J}_y)/2$ are the jump operators, and γ_c is the dissipation rate. As $A = 0$ and then $\Gamma(t) = \Gamma_0$ is a constant, the solution of Eq. (2) was studied previously [23]. The jump operator forces the spins to be aligned in the negative z direction, while the interaction between spins favors an alignment in the x direction. Their interplay results in a steady state, which is either ferromagnetic (with nonzero magnetization in the x direction) or paramagnetic. Here we extend to the case of $A \neq 0$, in which the field oscillation prevents a steady state being reached, and then we expect a nontrivial dynamical behavior.

III. CHAOTIC DYNAMICS IN THE MEAN-FIELD EQUATIONS

The mean-field theory is frequently employed for solving the all-to-all models [16,18,19,22,23,25–27,60,61]. We choose the order parameters to be $m_\alpha = \langle \hat{J}_\alpha \rangle = \text{Tr}[\hat{\rho} \hat{J}_\alpha]$. By ignoring the correlations (i.e., setting $\langle \hat{J}_\alpha \hat{J}_\beta \rangle = \langle \hat{J}_\alpha \rangle \langle \hat{J}_\beta \rangle$) in the limit $N \rightarrow \infty$, we obtain a nonlinear system of differential equations, which read

$$\begin{aligned} \dot{m}_x &= -2\Gamma(t)m_y + \gamma_c m_x m_z, \\ \dot{m}_y &= 4m_x m_z + 2\Gamma(t)m_x + \gamma_c m_y m_z, \\ \dot{m}_z &= -4m_x m_y - \gamma_c(m_x^2 + m_y^2). \end{aligned} \quad (3)$$

It is easy to see that $|\mathbf{m}(t)| = \sqrt{m_x^2 + m_y^2 + m_z^2}$ is a constant of motion, which can be set to unity without loss of generality.

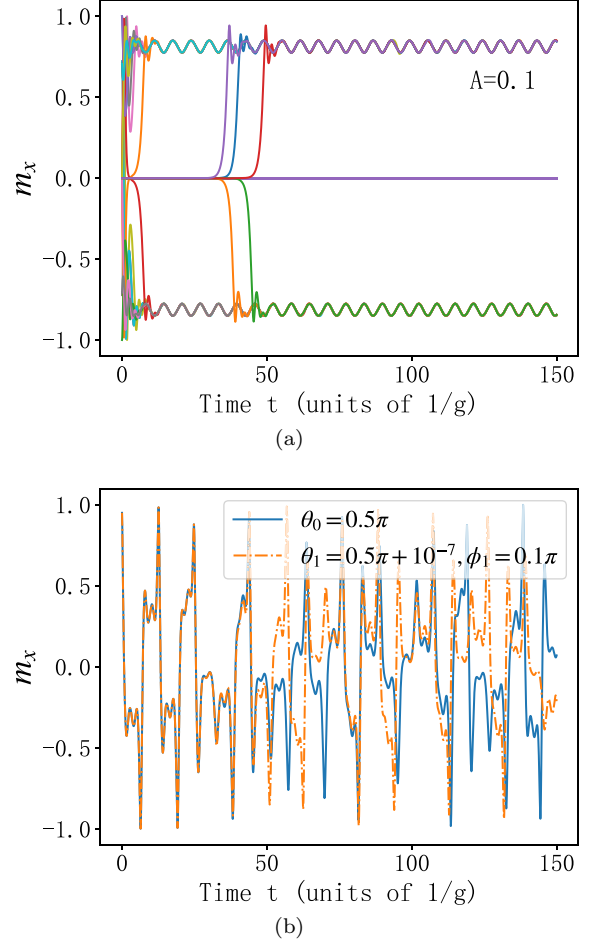


FIG. 1. The time evolution of m_x for (a) $A = 0.1$ with 25 different initial states and (b) $A = 1$ with two initial states: $(\theta_0 = 0.5\pi, \phi_0 = 0.1\pi)$ and $(\theta_1 = 0.5\pi + 10^{-7}, \phi_1 = 0.1\pi)$. Different line colors are for different initial states. The dissipation strength is set to $\gamma_c = 1$.

\mathbf{m} is moving on a Bloch sphere, and the initial state can be described by the azimuthal angles (θ, ϕ) , which are defined by $m_x = \sin \theta \cos \phi$, $m_y = \sin \theta \sin \phi$, and $m_z = \cos \theta$. Equivalently speaking, we force all the spins at the initial time to be aligned in the same direction, i.e., the direction with azimuthal angles (θ, ϕ) .

Since the coefficient $\Gamma(t)$ is a periodic function of t with the period $2\pi/\omega_0$, one may naively think that the solution $\mathbf{m}(t)$ is also a periodic function. This is the case for small A , but not true for large A . We note that Eq. (3) bears some resemblance to the Lorenz equation [62], one famous example of the deterministic chaos in the classical systems. In Eq. (3), the possibility of chaos comes from the fact that $\Gamma(t)$ is time periodic [63], even the trajectory is limited on a two-dimensional sphere. Indeed, we observed a periodic $\mathbf{m}(t)$ for small A , but a chaotic $\mathbf{m}(t)$ for large A . Something similar has been observed in the Rabi Hamiltonian, which is integrable over the entire parameter space [64,65]. But when an external drive is introduced, the system can become chaotic at some specific driving amplitudes [63].

Next we choose $\Gamma_0 = 1$ and $\omega = 1$ as an example for the demonstration. In Fig. 1(a), we display the evolution of m_x for small A ($A = 0.1$) and 25 initial states that are evenly

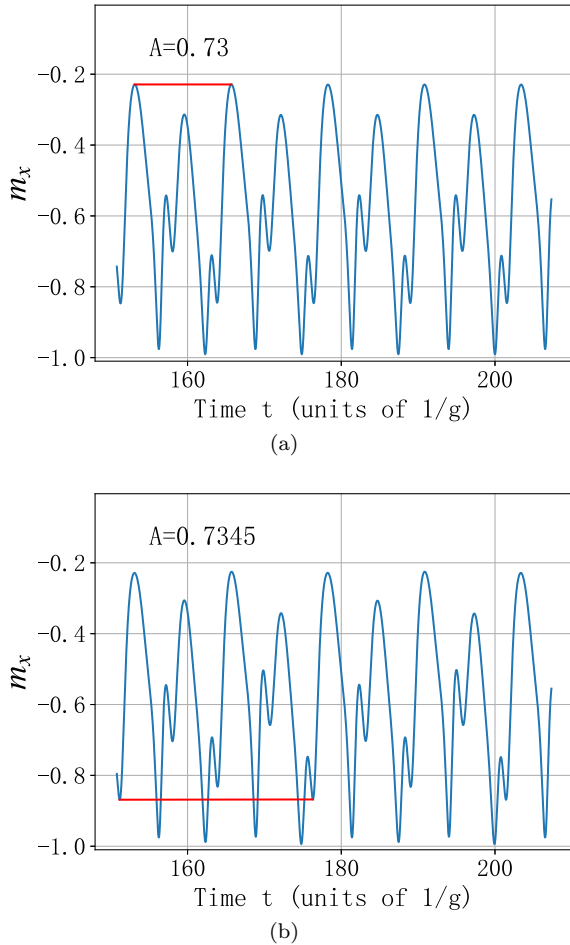


FIG. 2. The time evolution of m_x for (a) $A = 0.73$ and (b) $A = 0.7345$. The red line highlights a complete period. The transient regime ($t < 150$) is omitted.

distributed on the Bloch sphere. We find that the results with different initial states are similar with no significant difference in the long-term dynamical behavior. The choice of initial state does not affect whether the dynamics has an initial-state sensitivity. Except for the initial state at the south pole [$\mathbf{m} = (0, 0, 1)$], all the others eventually evolve into one of the two oscillation modes that are symmetric to each other. The two

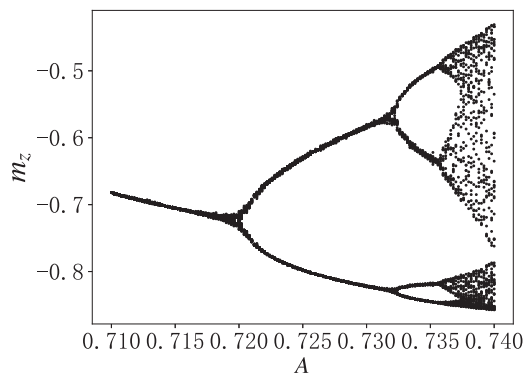


FIG. 3. Bifurcation diagram of the stroboscopic values of m_z as a function of A , as $\gamma = 1$.

oscillation modes have the same period, which is exactly the driving period ($2\pi/\omega_0$). For small A , the long-time response is insensitive to a small deviation in the initial state. On the other hand, Fig. 1(b) shows the evolution of m_x for a large A ($A = 1.0$). Without loss of generality, we choose the initial state to be $(\theta_1 = 0.5\pi, \phi_1 = 0.1\pi)$. Till the largest evolution time that is accessible, no periodicity is observed. More importantly, the long-time response is extremely sensitive to the initial condition. Even for a tiny deviation in the initial state ($\theta_1 - \theta_0 = 10^{-7}$), $m_x(t)$ displays a significant difference as t is as large as a few hundred [see the lines of different colors in Fig. 1(b)].

For the values of A between 0.1 and 1.0, $m_x(t)$ displays abundant dynamical behaviors. As A increases up to a certain critical value, the time period is doubled. In Fig. 2(a), we plot $m_x(t)$ for $A = 0.73$. It is easy to see that the period is not $2\pi/\omega_0$; instead, it becomes $4\pi/\omega_0$. As A increases further, the period doubling happens again. For example, for $A = 0.7345$, the period becomes $8\pi/\omega_0$ [see Fig. 2(b)]. The period-doubling bifurcation is well known in the classical nonlinear systems. Usually, a cascade of period-doubling bifurcations leads to chaos [66]. This explains why we observe a chaotic dynamics as A is as large as $A = 1$.

To further clarify the bifurcation and development of chaos, we evolve Eq. (3) from randomly chosen initial conditions, and, after a transient period of length $16T$, record the values of m_z at the next 100 stroboscopic instants of time. The obtained bifurcation diagram is presented in Fig. 3. As the oscillating amplitude A increases, we observe the period doubling and chaotic attractors. We provide more evidence for the existence of different dynamical behaviors in the Appendix, where the trajectory of $\mathbf{m}(t)$ on the Bloch sphere is plotted.

In our model, the subharmonic response (i.e., doubled period) to a time-periodic Liouvillian must be distinguished from that in the Floquet time crystals. As will be shown next, the subharmonic response in our model can only be observed in the mean-field limit. It cannot survive the quantum fluctuation that is unavoidable at finite N . To locate the chaotic phase in the parameter space, we calculate the Lyapunov exponent. The defining property of a chaotic system is the extreme sensitivity of trajectories to the initial condition. Two points that are initially close will drift apart exponentially over time. The Lyapunov exponent [67] provides a quantitative measure for this, which is defined as the average exponential rate of convergence or divergence between adjacent trajectories in the phase space. Especially, the largest Lyapunov exponent (LLE) is frequently employed for determining whether a nonlinear system is chaotic. If the LLE is greater than zero, two initial points will depart from each other exponentially, and then the system is chaotic [68]; otherwise, it is not. We use the Wolf algorithm for obtaining the Lyapunov exponents. Figure 4 displays the dependence of the LLE on A and γ_c . The area in red or yellow has a positive LLE, while the area in blue or green has a negative LLE. The chaotic phase is clearly distinguishable in the parameter space. An interesting finding is that for a fixed γ_c in the interval $(0, 1)$, the dynamics is chaotic only for an intermediate amplitude of oscillating field, but the dynamics is regular either if A is too large or too small. In the presence of

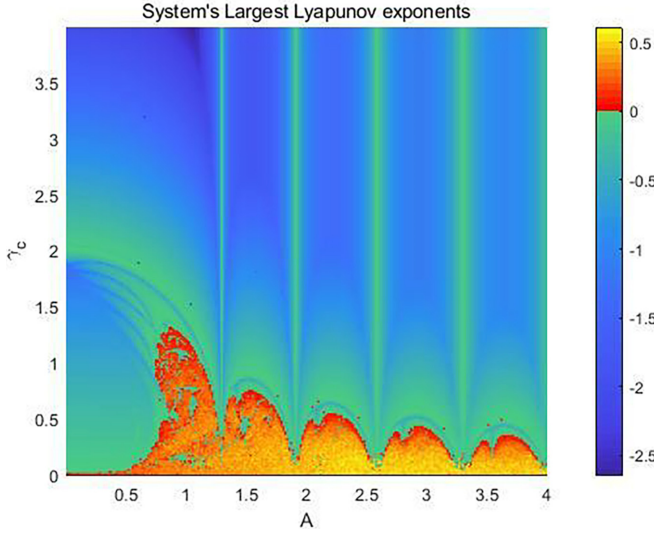


FIG. 4. The largest Lyapunov exponent as a function of γ_c and A . The system displays chaotic dynamics as $LLE > 0$ (see the area in red or yellow).

strong dissipation ($\gamma_c > 1.5$), there is no chaotic dynamics for whatever A .

IV. PERIODIC BEHAVIOR AT FINITE N

The mean-field result is usually called the classical limit in the study of quantum chaos. Next, to check the validity of mean-field approximation, we numerically simulate the real-time dynamics at finite N , by exploiting the permutation symmetry of all-to-all models. The Dicke basis with maximum angular momentum is defined as [69]

$$|M\rangle = \sqrt{\frac{1}{C_N^{\frac{N}{2}+M}}} \sum_{\sum_{j=1}^N \sigma_j = M} |\sigma_1, \sigma_2, \dots, \sigma_N\rangle, \quad (4)$$

where $C_N^{\frac{N}{2}+M}$ is the binomial coefficient, and $\sigma_j = \pm 1/2$ represents the spin-up and down states, respectively. And $M = -N/2, -N/2 + 1, \dots, N/2$ is the magnetization in the z direction. The initial state is supposed to be a pure state with all the spins aligned in the same direction. We use the azimuthal angles (θ, ϕ) to indicate the initial direction, then the initial state can be expressed in the Dicke basis as

$$|\theta, \phi\rangle = \sum_{M=-\frac{N}{2}}^{\frac{N}{2}} C_N^{M+\frac{N}{2}} \cos \frac{\theta}{2}^{\frac{N}{2}+M} \sin \frac{\theta}{2}^{\frac{N}{2}-M} e^{i(\frac{N}{2}-M)\phi} |M\rangle. \quad (5)$$

Equation (2) has permutation symmetry; its solution can then be expressed as $\hat{\rho}(t) = \sum_{M, M'} \rho_{M, M'}(t) |M\rangle \langle M'|$, where $\rho_{M, M'}(t)$ is the density matrix in the Dicke basis. Now Eq. (2) changes into a system of ordinary differential equations for $\rho_{M, M'}$, which are solved numerically. The permutation symmetry reduces the dimension of Hilbert space from 2^N to N , and then allows us to access a large system with the number of spins $N \approx 10^2 - 10^3$.

In Fig. 5(a), we compare the dynamics of magnetizations at finite N and in the mean-field approximation ($N = \infty$),

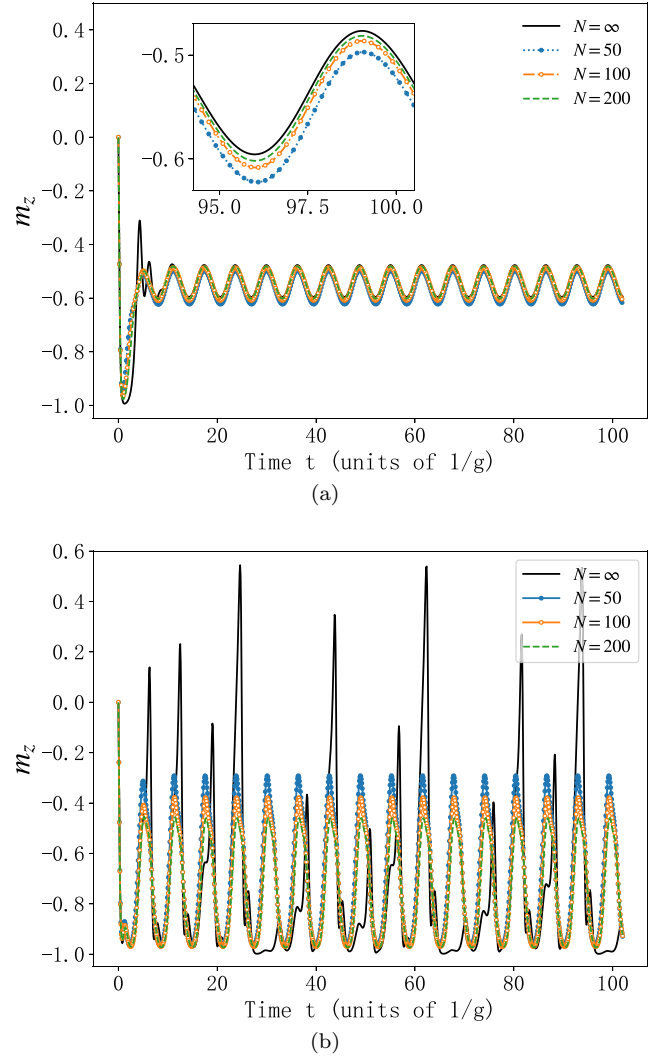


FIG. 5. The time evolution of m_z for (a) $A = 0.1$ and (b) $A = 1$ with different N . The black solid lines represent the mean-field results. The initial condition is fixed to be $\theta_0 = 0.5\pi$, $\phi_0 = 0.2\pi$.

as $A = 0.1$ is in the mean-field periodic regime. At finite N , the magnetizations display periodic oscillations in the asymptotic long time. The curve of $m_z(t)$ at $N = 50$ is already very close to the mean-field one. As N increases, $m_z(t)$ goes even closer to the mean-field result [see Fig. 5(a) inset]. As $N \rightarrow \infty$, we expect that the numerical results should coincide with the mean-field results. If A is small, then the mean-field approximation is good for large enough N .

Figure 5(b) shows the comparison as $A = 1.0$ is in the mean-field chaotic regime. The results are significantly different from those at $A = 0.1$. Up to $N = 200$, we find no similarity between the numerical result and the mean-field one. For N ranging between 50 and 200, the initial transient behavior of $m_z(t)$ always quickly evolves into the asymptotic behavior: periodic oscillation. And the $m_z(t)$ for $N = 50$ and 200 have the same period, with only their amplitude being different. But in the mean-field result, $m_z(t)$ is aperiodic at arbitrarily long time. These observations suggest that the exact numerical solutions do not converge to the mean-field

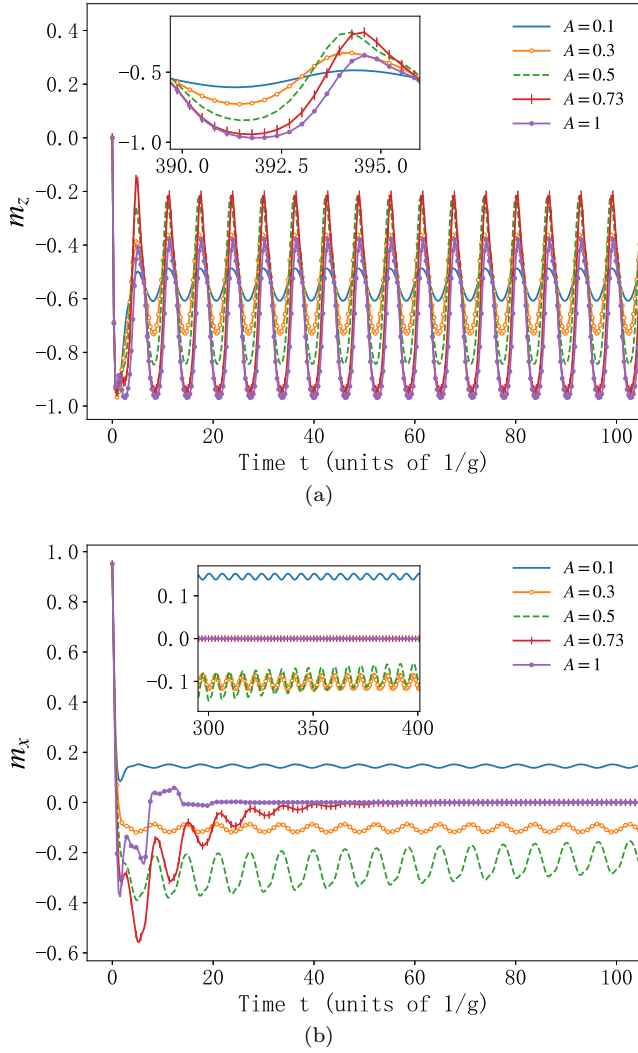


FIG. 6. The evolution of m_x and m_z with different A . The number of spins is chosen to be $N = 100$. And the initial condition is $\theta_0 = 0.5\pi$, $\phi = 0.1\pi$.

one in the limit $N \rightarrow \infty$. If A is large, then the mean-field approximation is bad, even for large N . This seems to be strange for an all-to-all model. We will further discuss this discrepancy in next section. We also compare the dynamics of magnetizations for different A , as N is fixed. Figures 6(a) and 6(b) display $m_z(t)$ and $m_x(t)$, respectively, for the values of A ranging from 0.1 to 1.0. The magnetization in the z direction always displays a periodic oscillation. And the oscillations for different A are in phase [see Fig. 6(a) inset]. On the other hand, the magnetization in the x direction displays two different dynamical modes, depending on the value of A . As seen in Fig. 6(b), as A is small ($A = 0.1, 0.3$), m_x displays an everlasting oscillation with the period $2\pi/\omega_0$. But as A is large ($A = 0.73, 1.0$), m_x rapidly decays to zero. For an intermediate A ($A = 0.5$), m_x maintains an oscillation for a relatively long time, but the decay can still be clearly seen. Since the mean-field approximation conserves $|\mathbf{m}|$, m_x should remain finite at arbitrarily large time (see the Appendix). The decay of m_x is a signal that the quantum result deviates from the mean-field approximation.

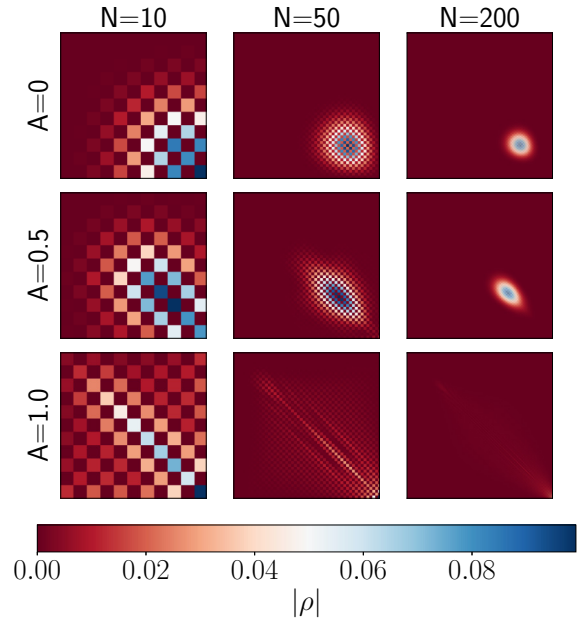


FIG. 7. Absolute values of the density-matrix elements for different A .

V. DENSITY-MATRIX ELEMENTS

The discrepancy between mean-field approximation and finite- N simulation needs an explanation. Indeed, the possibility of replacing Eq. (2) in terms of the classical equations (3) relies on the fact that the wave packet is of small width ($\approx 1/\sqrt{N}$) [69]. This means that, in the presence of dissipation, the density matrix $\langle M|\hat{\rho}|M'\rangle$ should display a sharp peak of width $\approx 1/\sqrt{N}$ in the $\frac{M}{N}-\frac{M'}{N}$ plane.

Previous simulations tell us that the periodic behavior emerges for $t > 40$; therefore, we choose to plot the density matrix at $t = 100 \gg 40$. Figure 7 shows the density-matrix elements in the $\frac{M}{N}-\frac{M'}{N}$ plane, for different values of A . As $A = 0$ or 0.5 , the density matrix displays a peak structure. The nonzero matrix elements concentrate within an elliptical region, and the area of concentration decreases with N . For N as large as 100, we clearly see the localization of nonzero matrix elements. It is reasonable to think that all the nonzero elements will be localized into a single point in the limit $N \rightarrow \infty$, in which limit the classical mean-field theory is valid. On the other hand, the paradigm for $A = 1.0$ is qualitatively different. The density matrix does not display a peak structure. Instead, the nonzero elements disperse widely in the whole $\frac{M}{N}-\frac{M'}{N}$ plane. As N increases, there is no significant concentration of the nonzero elements. This means that the foundation of mean-field approximation collapses as $A = 1.0$. A discrepancy between mean-field approximation and finite- N result is then expected.

We notice that, for a single particle trapped in a harmonic potential, some studies [56–58] showed that the dissipation tends to localize the wave packet and then the $N \rightarrow \infty$ limit coincides with the mean-field approximation. But in the current model, the dissipation does not result in localization. This difference will be further discussed next.

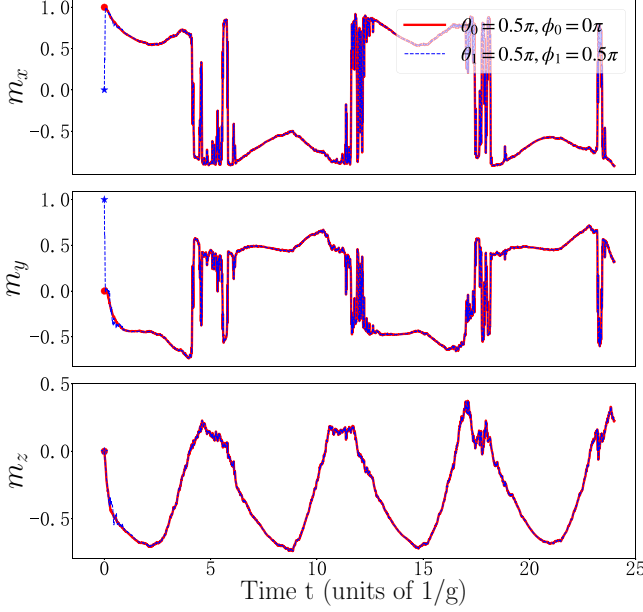


FIG. 8. The quantum trajectories of $\mathbf{m}(t)$, generated by the unraveled equation. We choose $A = 1.0$ and $N = 100$.

VI. UNRAVELING OF THE MASTER EQUATION AND QUANTUM TRAJECTORIES

It is possible to transform the Lindblad equation (2) into a stochastic differential equation by an approach called *unraveling*, resulting in [58]

$$|d\psi\rangle = -i\hat{H}|\psi\rangle dt + \sqrt{2N\gamma_c}(\hat{J}_- - \langle\hat{J}_-\rangle)|\psi\rangle d\xi_t + 2N\gamma_c(\langle\hat{J}_+\rangle\hat{J}_- - \frac{1}{2}\hat{J}_+\hat{J}_- - \frac{1}{2}\langle\hat{J}_+\rangle\langle\hat{J}_-\rangle)|\psi\rangle dt, \quad (6)$$

where $d\xi_t = (d\xi_t^R + id\xi_t^I)/\sqrt{2}$ with ξ_t^R and ξ_t^I denoting two independent Wiener processes. Equation (6) describes a random motion of $|\psi\rangle$ in the Hilbert space. By ordering $\hat{\rho} = |\psi\rangle\langle\psi|$ where $\langle\cdots\rangle$ denotes the average over the distribution of ξ_t , we recover the master equation (2). The unraveled equation (6) is sometimes used in the numerical simulation, replacing the original master equation, since the dimension of Hilbert space is much less than that of the density matrix. Equation (6) was also employed in the study of quantum chaos [58], in which it provides a direct comparison between quantum trajectories and classical trajectories, while the original Lindblad equation only provides a comparison between quantum expectation values and classical trajectories.

We numerically solve Eq. (6) to obtain the corresponding $m_\alpha = \langle\hat{J}_\alpha\rangle = \langle\psi|\hat{J}_\alpha|\psi\rangle$. Figure 8 illustrates the random evolution of magnetization for two different initial states, $(\theta_0 = 0.5\pi, \phi_0 = 0\pi)$ and $(\theta_1 = 0.5\pi, \phi_1 = 0.5\pi)$, induced by the same path ξ_t . We choose $A = 1.0$ to be in the classical chaotic regime. We can see that the dynamical behavior with two different initial states is basically the same, and there is no initial-state sensitivity. Even if each single quantum trajectory is nonperiodic due to the random force, it does not exhibit initial-state sensitivity. This coincides with our previous results of expectation values, that is, the finite- N quantum dynamics of magnetizations does not exhibit chaos.

It will be interesting to compare our results with some previous studies of quantum chaotic dynamics. In Refs. [56,57], the jump operator is Hermitian, while the jump operator in Eq. (6) is $(\hat{J}_- - \langle\hat{J}_-\rangle)$, that is, non-Hermitian. In Ref. [58], the jump operator is also non-Hermitian, but the commutator between the jump operator and the driving term in \hat{H} is a constant, while in Eq. (6), the commutator is $[\hat{J}_-, \hat{J}_z]$, that is, not a constant. These differences might be responsible for the different destiny of the wave packet. In our model, the wave packet is delocalized, as shown in the previous section; therefore, the mean-field approximation fails, even if we consider the stochastic quantum trajectory. But the wave packet is localized by the jump operator in previous studies.

VII. FLOQUET LIOUVILLIAN SPECTRUM

In a closed system, it is widely believed that the mean-field approximation becomes exact for the all-to-all models in the limit $N \rightarrow \infty$. In the open systems, a similar result was obtained [70], as the Liouvillian is time independent. But our numerical results suggest that the mean-field approximation is bad even in the limit $N \rightarrow \infty$, if there is a big time-periodic term in the Liouvillian and the classical equations display chaotic features. Since we can only obtain the exact results at finite N , a scaling analysis is helpful for confirming our viewpoint. Next we give a scaling analysis of the Floquet Liouvillian spectrum. The Lindblad equation can be expressed in a vectorized form as

$$\frac{d\hat{\rho}}{dt} = \hat{\mathcal{L}}(\hat{\rho}), \quad (7)$$

where $\hat{\mathcal{L}}$ is the so-called Liouvillian superoperator (or Liouvillian in short), which is a non-Hermitian linear operator acting on the vector space of density matrices. For the dissipative systems with time-independent $\hat{\mathcal{L}}$, it is well known that the eigenvalues and eigenvectors of $\hat{\mathcal{L}}$ determine the dynamics. The eigenvalues of $\hat{\mathcal{L}}$ (Liouvillian spectrum) are complex numbers. More important, if the system size N is finite, all the eigenvalues must have negative real part, except one that is zero.

These notations can be generalized to the case of time-periodic $\hat{\mathcal{L}}$. For a Lindblad equation with $\hat{\mathcal{L}}(t) = \hat{\mathcal{L}}(t + T)$, there exists a complete set of solutions written as $\hat{\rho}(t) = e^{\lambda t} \hat{\rho}(t)$, where $\hat{\rho}(t) = \hat{\rho}(t + T)$ is the time-periodic part of the density matrix, according to the Floquet theorem. And $\hat{\rho}(t)$ satisfies

$$\hat{\mathcal{L}}[\hat{\rho}(t)] - \frac{d}{dt}\hat{\rho}(t) = \lambda\hat{\rho}(t). \quad (8)$$

Then λ can be seen as the eigenvalue of $[\hat{\mathcal{L}}(t) - d/dt]$, which is an operator acting on the generalized vector space of density matrices, just as $(\hat{H} - id/dt)$ is an operator acting on the generalized Hilbert space (Sambe space) for a closed system with time-periodic Hamiltonian. While the eigenvalues of $(\hat{H} - id/dt)$ are called the Floquet spectrum, the eigenvalues of $[\hat{\mathcal{L}}(t) - d/dt]$ are called the Floquet Liouvillian spectrum.

We can formally define the Floquet Liouvillian as follows. The evolution superoperator that maps $\hat{\rho}(t_0)$ at some reference time (denoted by t_0) to $\hat{\rho}(t_0 + T)$ can be

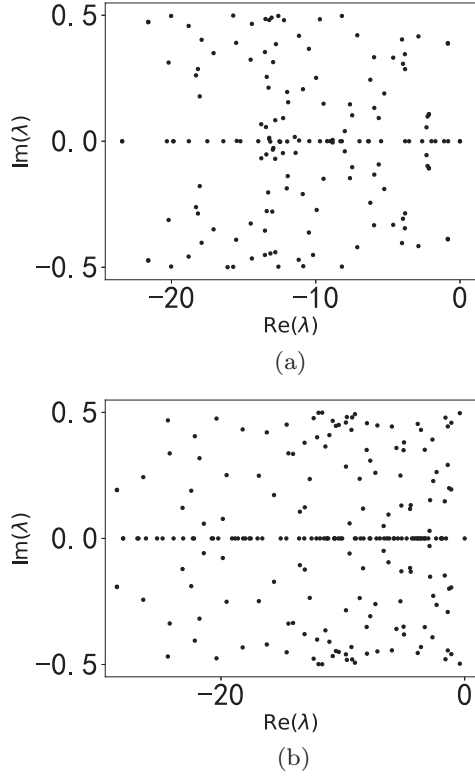


FIG. 9. The Floquet Liouvillian spectrum for (a) $A = 0.1$ and (b) $A = 1.0$. The number of spins is $N = 30$.

written as $\hat{P}_{t_0} = \mathcal{T} \exp\{\int_{t_0}^{t_0+T} dt \hat{\mathcal{L}}(t)\}$, where \mathcal{T} represents the time ordering. Then, $\hat{\varrho}(t_0)$ in Eq. (8) is the eigenvector of \hat{P}_{t_0} , with the corresponding eigenvalue being $e^{\lambda T}$. The Floquet Liouvillian can be defined as $\hat{S}_{t_0} = \ln \hat{P}_{t_0}/T$, whose eigenvectors and eigenvalues are $\hat{\varrho}(t_0)$ and λ , respectively. The Floquet Liouvillian spectrum is indeed the spectrum of \hat{S}_{t_0} . It is worth emphasizing that \hat{S}_{t_0} does not necessarily have a Lindblad form [31,71]. The criteria for judging whether \hat{S}_{t_0} is Lindbladian were given in Ref. [71]. And it was found that \hat{S}_{t_0} is non-Lindbladian for some parameters of a few-body open system [31]. Checking whether \hat{S}_{t_0} is Lindbladian is particularly difficult for a many-body system like ours, because the logarithmic function has an infinite number of branches in the complex plane. We only find that \hat{S}_{t_0} does not have a Lindblad form in the principal branch. But, whether \hat{S}_{t_0} is Lindbladian is unimportant for the analysis of the spectrum. As will be shown next, it is the properties of the spectrum that determine the periodic behavior in the dynamics.

Numerically, we obtain the Floquet Liouvillian spectrum by diagonalizing the matrix of $[\hat{\mathcal{L}}(t) - d/dt]$ in the generalized vector space of the density matrix. We decompose $\hat{\varrho}(t)$ into the linear combination of $e^{im\omega_0}|M\rangle\langle M'|$, where $\{|M\rangle\langle M'|\}$ spans the density-matrix space, $\omega_0 = 2\pi/T$ is the driving frequency, and $m = 0, \pm 1, \pm 2, \dots$ indexes different photon blocks. Equation (8) then changes into a matrix equation. We need to cut off the range of m for a numerical diagonalization. In practice, keeping more than ten blocks realizes a good

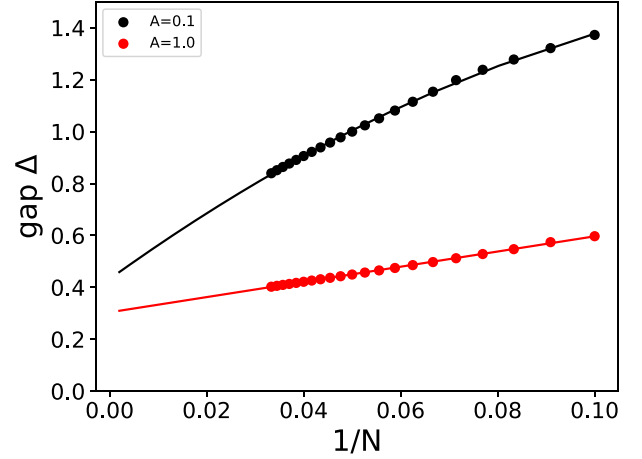


FIG. 10. The Floquet Liouvillian gap as a function of $1/N$. The dots represent the numerical results, while the lines represent the fitted curves.

convergence in the spectrum. Note that such a technique is already well known in the studies of Floquet Hamiltonian systems [72].

Compared to the Floquet spectrum or Liouvillian spectrum, much less is known about the Floquet Liouvillian spectrum. For the dissipative systems, we guess that the Floquet Liouvillian spectrum has the same properties as the Liouvillian spectrum, i.e., all the complex eigenvalues have negative real parts except for a unique one that is zero. The numerics support our guess. Figure 9 displays the Floquet Liouvillian spectrum at $N = 30$. For both $A = 0.1$ and 1.0 , we see that the rightmost eigenvalue in the complex plane is zero, which is nondegenerate. And the others are to the left of zero, i.e., they have a negative real part.

The Floquet Liouvillian spectrum completely determines whether the dynamics is periodic, subharmonic, or chaotic. To see it, we arrange all the eigenvalues as

$$\lambda_0 = 0 \geq \text{Re}\lambda_1 \geq \text{Re}\lambda_2 \geq \dots, \tag{9}$$

with the corresponding eigenvectors being $\hat{\varrho}_0(t)$, $\hat{\varrho}_1(t)$, $\hat{\varrho}_2(t)$, \dots . For an arbitrary initial state, the solution of the Lindblad equation can be formally expressed as

$$\hat{\rho}(t) = \sum_j K_j e^{\lambda_j t} \hat{\varrho}_j(t), \tag{10}$$

where the coefficients K_j depend on the initial state. In the asymptotic long time, the terms with $\text{Re}\lambda_j < 0$ all decay to zero, and $1/|\text{Re}\lambda_j|$ is just the decay time of the j th mode. At finite N , all the λ_j with $j > 0$ have negative real parts; therefore, the density matrix in the asymptotic long time becomes

$$\hat{\rho}(t) \xrightarrow{t \rightarrow \infty} K_0 \hat{\varrho}_0(t), \tag{11}$$

which is exactly periodic with the period T . We then expect that the asymptotic behavior is always periodic at finite N . The situation is more complicated in the thermodynamic limit. As found in the previous studies of time-independent Liouvillians, there exist possibilities that the real parts of some λ_j decrease with increasing N and vanish in the limit $N \rightarrow \infty$

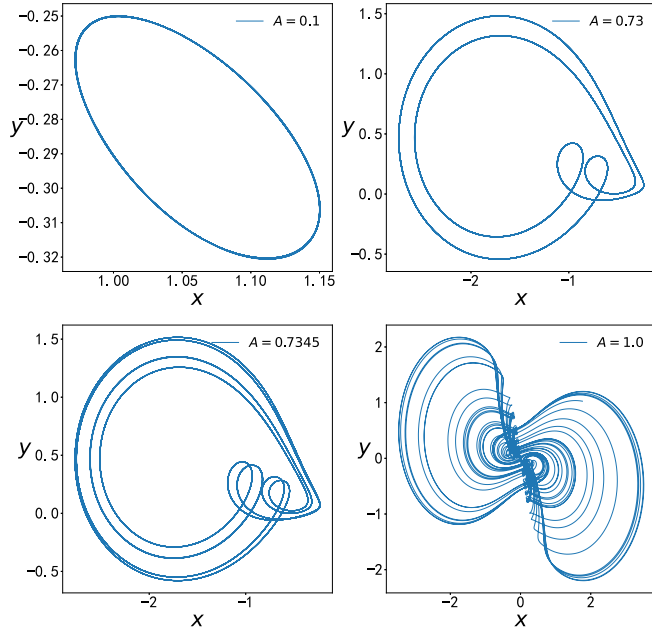


FIG. 11. The trajectories of $\mathbf{m}(t)$ during $t \in [16T_0, 80T_0]$ with $T_0 = 2\pi/\omega_0$ being the time period, for $A = 0.1, 0.73, 0.7345$, and 1.0 . The initial condition is chosen to be $(\theta, \varphi) = (0.5\pi, 0.1\pi)$.

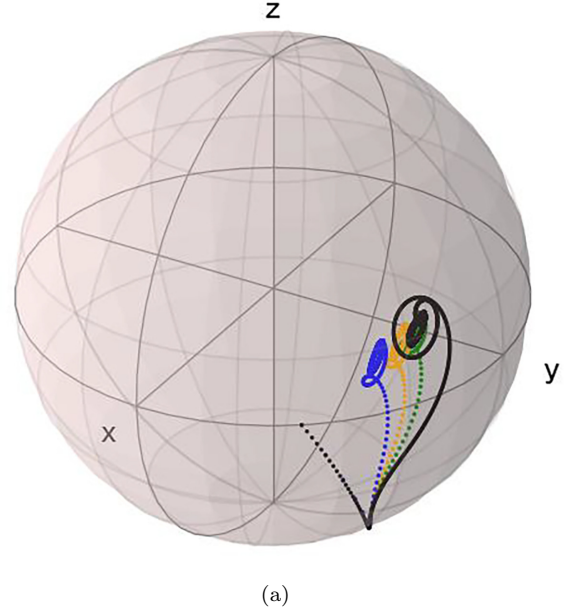
[11,18,61,73–76]. As a consequence, the asymptotic density matrix becomes

$$\hat{\rho}(t) \xrightarrow{t \rightarrow \infty} \sum_{j=0}^L K_j e^{i\text{Im}(\lambda_j)t} \hat{Q}_j(t), \quad (12)$$

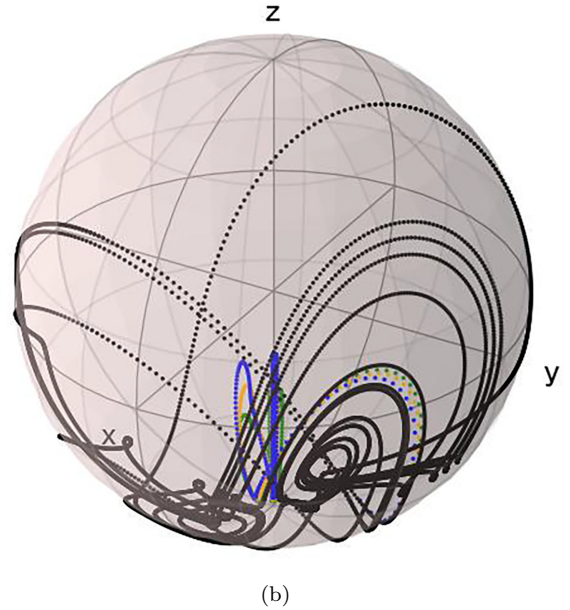
where L is the number of eigenvalues with vanishing real parts. Additionally, if these λ_j have also nonvanishing imaginary parts, then $\hat{\rho}(t)$ possibly display subharmonic or chaotic behaviors, depending on the values of $\text{Im}(\lambda_j)$. Conversely, if the real parts of λ_j with $j > 0$ are all finite in the limit $N \rightarrow \infty$, then subharmonic oscillation and chaotic behavior are both impossible. According to the above argument, we perform a scaling analysis of the Floquet Liouvillian gap, which is defined as $\Delta = \lambda_0 - \text{Re}\lambda_1$. If $\Delta \rightarrow 0$ in the thermodynamic limit, then there possibly exist multiple λ_j whose real parts vanish. But if Δ remains finite, then all the λ_j with $j > 0$ have negative real parts, and then Eq. (11) holds even in the thermodynamic limit. Figure 10 plots Δ as a function of $1/N$. The dots are the numerical results, while the lines are the fitted curves. The gap at $A = 1.0$ is smaller than the gap at $A = 0.1$. But in both cases, we clearly see that the gap does not go to zero as $N \rightarrow \infty$. The residue gaps in the limit $N \rightarrow \infty$ are comparable with the driving strength or driving frequency. This indicates that no λ_j with $j > 0$ has vanishing real parts; therefore, the asymptotic behaviors are periodic for both $A = 0.1$ and 1.0 , even in the limit $N \rightarrow \infty$. Such a result is consistent with our previous simulation of the real-time dynamics of magnetizations.

VIII. CONCLUSIONS

In summary, we study the all-to-all Ising model with a time-periodic external field and subject to a dissipation,



(a)



(b)

FIG. 12. The trajectories of magnetizations on the Bloch sphere for (a) $A = 0.1$ and (b) $A = 1$ with different N . The black solid lines represent the mean-field results.

by using both the mean-field approximation and the exact numerical simulation. If the field amplitude is small, both the mean-field approximation and the numerical simulation predict a perfect periodic oscillation of magnetizations. And the numerical results in the thermodynamic limit are consistent with the mean-field one.

As the field amplitude increases, the mean-field approximation predicts the period doublings or subharmonic oscillations, and a series of period doublings finally leads to the chaotic dynamics of magnetizations, which is confirmed by the calculations of Lyapunov exponents. In contrast, the numerical simulation shows that the magnetizations are always oscillating periodically, whatever the field amplitude

is. No subharmonic or chaotic dynamics is observed, even when we choose the number of spins to be as large as a few hundred in the simulation. We analyze the Floquet Liouvillian gap, which converges to a finite value in the thermodynamic limit, for either small or large field amplitude. A finite gap is another evidence of the periodic oscillations of observables.

To explain the failure of mean-field approximation, we study the density-matrix elements. As the driving amplitude is small, the density matrix displays a peak structure, with its width decreasing towards zero in the thermodynamic limit, indicating that the mean-field approximation works. But as the amplitude is large, the peak structure in the density matrix vanishes, indicating that the foundation of mean-field theory collapses.

We also study the unraveled stochastic equation, which gives the quantum trajectories of magnetizations. For both small and large amplitudes, the quantum trajectory does not show initial-state sensitivity.

For the all-to-all models, the mean-field approximation is generally believed to be good for sufficiently large number of spins. But we find that this is not the case if the time-periodic field and the dissipation are both present. For a large field amplitude, the predictions from the mean-field approximation and the numerical method are qualitatively different. Our finding suggests that one should be more careful when using the mean-field approximation in the case of time-periodic Liouvillians.

ACKNOWLEDGMENTS

P.W. is supported by the National Natural Science Foundation of China under Grants No. 11774315 and No. 11835011, and by the Junior Associates program of the Abdus Salam International Center for Theoretical Physics.

APPENDIX: TRAJECTORY ON THE BLOCH SPHERE

Because $|\mathbf{m}(t)|$ is a constant of motion in the mean-field equations, the vector $\mathbf{m} = (m_x, m_y, m_z)$ is moving on a Bloch sphere. Without loss of generality, we set $|\mathbf{m}| = 1$. For $|\mathbf{m}| \neq 1$, we can always rescale $|\mathbf{m}|$ to unity by changing the units.

To display the trajectory of $\mathbf{m}(t)$ on a sphere, we first perform the stereographic projection and map the unit sphere into the x - y plane. The map is defined by $x = 2m_x/(1 - m_z)$ and $y = 2m_y/(1 - m_z)$. Figure 11 displays the trajectories in the x - y plane for $A = 0.1, 0.73, 0.7345$, and 1.0 . We choose the time interval to be $[16T_0, 80T_0]$ with $T_0 = 2\pi/\omega_0$ being the period. The periodic, subharmonic, and chaotic behaviors are clearly distinguishable. As $A = 0.1$, the trajectory is periodic with an oval shape. As $A = 0.73$, the trajectory has two different loops, which is a signature of period doubling, as it should be. As $A = 0.7345$, the trajectory has four different loops, indicating that the period is four times that of the original one. As $A = 1.0$, we find the trajectory is aperiodic, showing features of chaos. From Fig. 11, we can also see that the three components are all nonzero; otherwise, the trajectory in the plane should be a circle or straight line.

Figure 12 displays the trajectories in the Bloch sphere for $A = 0.1$ and 1.0 with different N . The parameters are chosen to be the same as in Fig. 5. The black line represents the mean-field result. We see that the mean-field trajectory is on the unit sphere, because $m^2 = m_x^2 + m_y^2 + m_z^2$ is conserved. But the quantum trajectory at finite N does not conserve J^2 . As a consequence, the quantum trajectory does not stay on the unit sphere. As $A = 0.1$, the quantum trajectory goes closer to the mean-field one as N increases. But as $A = 1.0$, the difference between quantum and mean-field trajectories is always clear, even for large N . The mean-field trajectory displays a chaotic behavior on the sphere. But at finite N , the x and y components quickly decay to zero. Only m_z experiences a periodic oscillation.

-
- [1] S. Puri, C. K. Andersen, A. L. Grimsmo, and A. Blais, *Nat. Commun.* **8**, 15785 (2017).
 - [2] A. Clerk, K. Lehnert, P. Bertet, J. Petta, and Y. Nakamura, *Nat. Phys.* **16**, 257 (2020).
 - [3] K. Xu, Z.-H. Sun, W. Liu, Y.-R. Zhang, H. Li, H. Dong, W. Ren, P. Zhang, F. Nori, D. Zheng, H. Fan, and H. Wang, *Sci. Adv.* **6**, eaba4935 (2020).
 - [4] L. Henriot, L. Beguin, A. Signoles, T. Lahaye, A. Browaeys, G.-O. Raymond, and C. Jurczak, *Quantum* **4**, 327 (2020).
 - [5] J. Zeiher, J.-Y. Choi, A. Rubio-Abadal, T. Pohl, R. van Bijnen, I. Bloch, and C. Gross, *Phys. Rev. X* **7**, 041063 (2017).
 - [6] H. Labuhn, D. Barredo, S. Ravets, S. De Léséleuc, T. Macrì, T. Lahaye, and A. Browaeys, *Nature (London)* **534**, 667 (2016).
 - [7] M. Saffman, T. G. Walker, and K. Mølmer, *Rev. Mod. Phys.* **82**, 2313 (2010).
 - [8] A. Angerer, K. Streltsov, T. Astner, S. Putz, H. Sumiya, S. Onoda, J. Isoya, W. J. Munro, K. Nemoto, J. Schmiedmayer, and J. Majer, *Nat. Phys.* **14**, 1168 (2018).
 - [9] J. Zhang, G. Pagano, P. W. Hess, A. Kyprianidis, P. Becker, H. Kaplan, A. V. Gorshkov, Z.-X. Gong, and C. Monroe, *Nature (London)* **551**, 601 (2017).
 - [10] H.-P. Breuer and F. Petruccione, *The Theory of Open Quantum Systems* (Oxford University Press, New York, 2002).
 - [11] E. M. Kessler, G. Giedke, A. Imamoglu, S. F. Yelin, M. D. Lukin, and J. I. Cirac, *Phys. Rev. A* **86**, 012116 (2012).
 - [12] T. E. Lee, H. Häffner, and M. C. Cross, *Phys. Rev. A* **84**, 031402(R) (2011).
 - [13] T. E. Lee, H. Häffner, and M. C. Cross, *Phys. Rev. Lett.* **108**, 023602 (2012).
 - [14] C. Ates, B. Olmos, J. P. Garrahan, and I. Lesanovsky, *Phys. Rev. A* **85**, 043620 (2012).
 - [15] A. Hu, T. E. Lee, and C. W. Clark, *Phys. Rev. A* **88**, 053627 (2013).
 - [16] M. Marcuzzi, E. Levi, S. Diehl, J. P. Garrahan, and I. Lesanovsky, *Phys. Rev. Lett.* **113**, 210401 (2014).
 - [17] H. Weimer, *Phys. Rev. Lett.* **114**, 040402 (2015).
 - [18] F. Iemini, A. Russomanno, J. Keeling, M. Schirò, M. Dalmonte, and R. Fazio, *Phys. Rev. Lett.* **121**, 035301 (2018).
 - [19] N. Shammah, S. Ahmed, N. Lambert, S. De Liberato, and F. Nori, *Phys. Rev. A* **98**, 063815 (2018).
 - [20] K. Tucker, B. Zhu, R. J. Lewis-Swan, J. Marino, F. Jimenez, J. G. Restrepo, and A. M. Rey, *New J. Phys.* **20**, 123003 (2018).

- [21] V. R. Overbeck, M. F. Maghrebi, A. V. Gorshkov, and H. Weimer, *Phys. Rev. A* **95**, 042133 (2017).
- [22] M. Foss-Feig, J. T. Young, V. V. Albert, A. V. Gorshkov, and M. F. Maghrebi, *Phys. Rev. Lett.* **119**, 190402 (2017).
- [23] P. Wang and R. Fazio, *Phys. Rev. A* **103**, 013306 (2021).
- [24] J. Jin, A. Biella, O. Viyuela, C. Ciuti, R. Fazio, and D. Rossini, *Phys. Rev. B* **98**, 241108(R) (2018).
- [25] T. E. Lee, S. Gopalakrishnan, and M. D. Lukin, *Phys. Rev. Lett.* **110**, 257204 (2013).
- [26] J. Jin, A. Biella, O. Viyuela, L. Mazza, J. Keeling, R. Fazio, and D. Rossini, *Phys. Rev. X* **6**, 031011 (2016).
- [27] D. Huybrechts, F. Minganti, F. Nori, M. Wouters, and N. Shammah, *Phys. Rev. B* **101**, 214302 (2020).
- [28] R. Rota, F. Storme, N. Bartolo, R. Fazio, and C. Ciuti, *Phys. Rev. B* **95**, 134431 (2017).
- [29] W. Casteels, R. M. Wilson, and M. Wouters, *Phys. Rev. A* **97**, 062107 (2018).
- [30] B. Zhu, J. Marino, N. Y. Yao, M. D. Lukin, and E. A. Demler, *New J. Phys.* **21**, 073028 (2019).
- [31] A. Schnell, A. Eckardt, and S. Denisov, *Phys. Rev. B* **101**, 100301(R) (2020).
- [32] A. Schnell, S. Denisov, and A. Eckardt, *Phys. Rev. B* **104**, 165414 (2021).
- [33] M. Hartmann, D. Poletti, M. Ivanchenko, S. Denisov, and P. Hänggi, *New J. Phys.* **19**, 083011 (2017).
- [34] I. Kamleitner and A. Shnirman, *Phys. Rev. B* **84**, 235140 (2011).
- [35] C. M. Dai, Z. C. Shi, and X. X. Yi, *Phys. Rev. A* **93**, 032121 (2016).
- [36] L. Magazzù, S. Denisov, and P. Hänggi, *Phys. Rev. E* **98**, 022111 (2018).
- [37] V. M. Bastidas, T. H. Kyaw, J. Tangpanitanon, G. Romero, L.-C. Kwek, and D. G. Angelakis, *New J. Phys.* **20**, 093004 (2018).
- [38] R. Dann, A. Levy, and R. Kosloff, *Phys. Rev. A* **98**, 052129 (2018).
- [39] A. C. Barato and R. Chetrite, *J. Stat. Mech.: Theory Exp.* (2018) 053207.
- [40] S. Scopa, G. T. Landi, and D. Karevski, *Phys. Rev. A* **97**, 062121 (2018).
- [41] F. Haake, M. Kuś, and R. Scharf, *Z. Phys. B* **65**, 381 (1987).
- [42] Q. Wang and M. Robnik, *Entropy* **23**, 1347 (2021).
- [43] U. T. Bhosale and M. S. Santhanam, *Phys. Rev. E* **95**, 012216 (2017).
- [44] J. N. Bandyopadhyay and A. Lakshminarayan, *Phys. Rev. E* **69**, 016201 (2004).
- [45] J. B. Ruebeck, J. Lin, and A. K. Pattanayak, *Phys. Rev. E* **95**, 062222 (2017).
- [46] M. Lombardi and A. Matzkin, *Phys. Rev. E* **83**, 016207 (2011).
- [47] X. Wang, S. Ghose, B. C. Sanders, and B. Hu, *Phys. Rev. E* **70**, 016217 (2004).
- [48] J. Iwaniszewski and P. Peplowski, *J. Phys. A* **28**, 2183 (1995).
- [49] S. Chaudhury, A. Smith, B. Anderson, S. Ghose, and P. S. Jessen, *Nature (London)* **461**, 768 (2009).
- [50] V. R. Krithika, V. S. Anjusha, U. T. Bhosale, and T. S. Mahesh, *Phys. Rev. E* **99**, 032219 (2019).
- [51] C. Neill, P. Roushan, M. Fang, Y. Chen, M. Kolodrubetz, Z. Chen, A. Megrant, R. Barends, B. Campbell, B. Chiaro *et al.*, *Nat. Phys.* **12**, 1037 (2016).
- [52] G. Engelhardt, V. M. Bastidas, C. Emary, and T. Brandes, *Phys. Rev. E* **87**, 052110 (2013).
- [53] A. Lerose, J. Marino, A. Gambassi, and A. Silva, *Phys. Rev. B* **100**, 104306 (2019).
- [54] A. Das, K. Sengupta, D. Sen, and B. K. Chakrabarti, *Phys. Rev. B* **74**, 144423 (2006).
- [55] A. Russomanno, R. Fazio, and G. E. Santoro, *Europhys. Lett.* **110**, 37005 (2015).
- [56] S. Ghose, P. Alsing, I. Deutsch, T. Bhattacharya, S. Habib, and K. Jacobs, *Phys. Rev. A* **67**, 052102 (2003).
- [57] S. Ghose, P. Alsing, I. Deutsch, T. Bhattacharya, and S. Habib, *Phys. Rev. A* **69**, 052116 (2004).
- [58] B. Pokharel, M. Z. Misplon, W. Lynn, P. Duggins, K. Hallman, D. Anderson, A. Kapulkin, and A. K. Pattanayak, *Sci. Rep.* **8**, 2108 (2018).
- [59] D. Manzano, *Aip Adv.* **10**, 025106 (2020).
- [60] J. Kurchan, P. Leboeuf, and M. Saraceno, *Phys. Rev. A* **40**, 6800 (1989).
- [61] G. Piccitto, M. Wauters, F. Nori, and N. Shammah, *Phys. Rev. B* **104**, 014307 (2021).
- [62] E. N. Lorenz, *J. Atmos. Sci.* **20**, 130 (1963).
- [63] J. Larson and D. H. J. O'Dell, *J. Phys. B* **46**, 224015 (2013).
- [64] D. Braak, *Phys. Rev. Lett.* **107**, 100401 (2011).
- [65] J. Larson and T. Mavrogordatos, *The Jaynes-Cummings Model and its Descendants* (IOP, Bristol, England, 2021).
- [66] D. Kaplan and L. Glass, *Understanding Nonlinear Dynamics* (Springer, New York, 1995).
- [67] J. P. Eckmann and D. Ruelle, *Rev. Mod. Phys.* **57**, 617 (1985).
- [68] A. Wolf, J. B. Swift, H. L. Swinney, and J. A. Vastano, *Physica D* **16**, 285 (1985).
- [69] B. Sciolla and G. Biroli, *J. Stat. Mech.* (2011) P11003.
- [70] F. Carollo and I. Lesanovsky, *Phys. Rev. Lett.* **126**, 230601 (2021).
- [71] M. M. Wolf, J. Eisert, T. S. Cubitt, and J. I. Cirac, *Phys. Rev. Lett.* **101**, 150402 (2008).
- [72] A. Eckardt and E. Anisimovas, *New J. Phys.* **17**, 093039 (2015).
- [73] V. V. Albert and L. Jiang, *Phys. Rev. A* **89**, 022118 (2014).
- [74] N. Shibata and H. Katsura, *Prog. Theor. Exp. Phys.* **2020**, 12A108 (2020).
- [75] Z. Cai and T. Barthel, *Phys. Rev. Lett.* **111**, 150403 (2013).
- [76] B. Baumgartner and H. Narnhofer, *J. Phys. A* **41**, 395303 (2008).